Method for the Sea Clutter Characterization in HF Surface Wave Radars From the Fields Diffracted by the Sea Surface

Omar Nova, Christophe Guiffaut, *Member, IEEE*, and Alain Reineix, *Member, IEEE*

***Abstract*—A new method for the characterization of the sea clutter in high-frequency surface wave radars is presented. The method is applied for the bistatic and the monostatic case. This method is based on the discretization of the sea surface in multiple patches. The fields diffracted by each patch are determined. Subsequently, the voltage that the diffracted fields induce on the receiving antenna is calculated. The sum of the voltages induced by all the patches is the sea clutter to be characterized. The fields diffracted by the sea patches are characterized in the form of field charts on a Huygens surface surrounding each patch. Field charts are modeled by analytical expressions. The current induced on the receiving antenna by the diffracted fields is calculated by means of the Lorentz reciprocity theorem. The feasibility of the method of characterization of the sea clutter is verified by means of the characterization of the fields diffracted by a single patch. The calculation of the induced current is done using the diffracted fields that are reconstructed from the analytical expressions that model them. It is also verified that the transmitting and receiving antenna can be replaced by plane wave sources, in order to simplify the calculations of the radiated fields that take part in the Lorentz reciprocity theorem. As a validation of the proposed method, the Doppler spectrum of a moving sea surface is calculated for the monostatic case.**

***Index Terms*—Diffracted fields, high-frequency surface wave radars (HFSWR), Huygens surface, Lorentz reciprocity theorem, scattering, sea clutter, sea surface.**

I. Introduction

FOR the maritime surveillance of the Exclusive Economic Zone (EEZ) of France, up to distances of 370 km from the coasts, high-frequency surface wave radars (HFSWR) are used [1]. The high-frequency (HF) band is chosen for these radars because at this frequency band, the radio range is greater. Nevertheless, in HF, the interference due to the sea clutter is greater as well. Hence, it is important to appropriately characterize the magnitude of the sea clutter. In the literature, the characterization of the sea clutter has been done through the calculation of the radar cross section (RCS) of the sea surface. To do it, statistical and analytical methods have been employed.

Manuscript received July 15, 2019; revised November 1, 2019; accepted December 24, 2019. Date of publication January 16, 2020; date of current version February 12, 2020. This work was supported in part by the ANR, the DGA, and the AID under the ANR ASTRID Maturation SimROS. *(Corresponding author: Omar Ariel Nova Manosalva.)*

The authors are with the Research Institute XLIM, UMR CNRS 7252, Limoges Cedex 87060, France (e-mail: omaranm@gmail.com; christophe.guiffaut@xlim.fr; alain.reineix@xlim.fr).

Digital Object Identifier 10.1109/JSTARS.2019.2963404

Among the statistical methods, we find the one developed by Barrick for monostatic case [2]–[4]. Then, this method was extended by Gill to the bistatic case [5]–[7]. In the method developed by Gill, first- and second-order RCS of the sea are considered. The first-order RCS is due to in-phase backscattering by Bragg waves. The second-order RCS appears due to the following two causes: in-phase backscattering by nonlinear waves of second order and two consecutive diffractions that lead to in-phase backscattering. The calculation of the second-order RCS has a high computational cost for finite sizes of the sea patch.

In [8]–[10], the power density of the RCS is calculated. Then, this power density must be converted to voltage at the terminals of the receiving antenna to obtain the sea clutter. In this article, the complex value of the voltage is directly computed from the fields diffracted by the sea surface. That is to say that we keep the phase information in our approach, which is not possible if the RCS is directly computed. Additionally, in the mentioned references, a statistical approach is used, in which the analysis of the RCS is divided into first and second order. In the current article, both orders are considered through the global analysis of the diffracted fields. The sea surface in [8]–[10] is considered of small height and slope, which limits the application to a little rough sea. On the contrary, the procedure proposed in this article can be applied to a sea surface with any degree of agitation because it does not make assumptions about the geometry of the surface (height and slope). In such a case, the only limitation comes from the sea model (Jonswap in the present case) that has to be modified for high level of agitation.

Among the analytical methods, we find the Kirchhoff approximation, the small perturbation method (SPM), the two scale method (TSM), and the small slope approximation (SSA). For all these methods, geometrical and physical characterization of the sea surface is required. The geometrical characterization is done by means of the height spectrum and the slope probability. The physical characterization is given by the permittivity and permeability of the sea medium [11], [12].

The Kirchhoff approximation [13]–[15], also known as tangent plane approximation, consists of considering the rough surface at any point as a plane tangent to that point. Therefore, this method can be applied under the following conditions: the mean curvature radius of the surface is greater than the incident wavelength and the surface has large roughness. The Kirchhoff approximation becomes less accurate as the angle of incidence

approaches grazing incidence. This is due to the shadowing of the incident wave because of the roughness of the surface.

When the roughness is small, the SPM is applied [14], [16], [17]. The SPM makes the formulation of the scattering problem as a boundary value problem based on partial differential equations. Through this formulation, it is possible to find the electric field as the sum of plane waves. Unlike the Kirchhoff approximation, the surface is no longer modeled as tangent planes at any point. This is possible because the SPM can only be applied in cases of small surface roughness, that is, low variation in the surface height and small slopes of the surface. The surface roughness is expanded in Fourier series and the field is found as the sum of the contributions of this expansion's components.

Since the Kirchhoff approximation is applicable on surfaces with large roughness and the SPM on surfaces with small roughness, it is desirable to find a method that can be applied for surfaces with large and small roughness, like those found in reality. These methods are TSM and SSA. The TSM [18]–[20] handles the large and small roughness by using two kinds of coordinate bases: several local bases for the small roughness and a global basis for the large roughness. The global basis is independent of the surface, while the local bases are dependent on it, since the z-direction of these bases coincides with the normal to the surface. The RCS for the small roughness is calculated by means of the SPM at the local bases. Then, all the RCS calculated in the local bases are projected on the global basis to obtain the final result. The global RCS is obtained by averaging the local RCSs over the surface slope probability. The TSM differentiates between a surface with large and small roughness by means of an arbitrary parameter. For this reason, the SSA arises, to make the transition between the two roughness scales in a smoother way.

The SSA [21]–[23] integrates the Kirchhoff approximation and the SPM without differentiating between large and small heights of the rough surface, but requiring the surface slope to be sufficiently small, which is true in many practical cases, including the case of the sea surface. In this way, the application range of the SPM is extended to surfaces with larger heights with small slope. When the slope is small, the scattering amplitude can be calculated by means of an asymptotic expansion in the surface slope parameter. After calculating the scattering amplitude, the value of the diffracted field can be determined. However, the SSA requires the slope parameter to be smaller than the grazing angle of the incident and diffracted waves [12], that is, the precision of the method decreases as the angle of the incident and diffracted waves increases.

As previously mentioned, our interest is the characterization of the sea clutter. The methods described in the previous paragraphs characterize the sea clutter by means of the calculation of the RCS, which is a parameter in terms of power or $|\mathrm{E}|^2$, from which the phase of the field cannot be recovered. The way in which we characterize the sea clutter requires the value in magnitude and phase of the diffracted E and H fields, in order to calculate the current induced in the receiving antenna, by the sum of the fields diffracted by all the sea patches in which the sea surface is divided. The SSA offers a way to calculate the diffracted field from the scattering amplitude. However, due to the decrease in the accuracy of the method as the incident and diffracted angle approaches the grazing angle, the SSA is not practical for the case of an HFSWR, in which the incident and diffracted waves propagate in grazing angles.

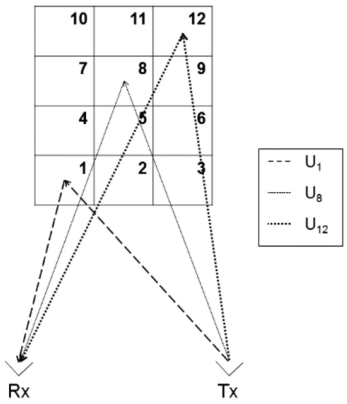

Fig. 1. Schematic representation of the sea patches distribution with three trajectories of the incoming and outgoing signals.

In Section II, the general procedure to characterize the sea clutter from the currents induced in the receiving antenna is presented. The way in which the induced current is calculated from the fields diffracted by each sea patch, through the Lorentz reciprocity theorem [24], is explained. In this section, the modeling by means of analytical expressions of the diffracted field charts around each patch is also discussed. Section III presents the results that validate the calculation principle of the induced current from the field charts reconstructed by using the analytical expressions of the model. The possibility of replacing transmitting and receiving antennas by plane wave sources is also validated, by verifying that the induced current result is not altered. This is necessary to simplify the calculation of the fields required in the Lorentz reciprocity theorem. To validate the computation procedure of the induced voltage on the receiving antenna, the Doppler spectrum of a moving sea surface is calculated. This spectrum is obtained as the Fourier transform of the time evolution of the induced voltage. The Bragg ray of the Doppler spectrum is obtained at the theoretically predicted frequency. Finally, conclusions and future work are presented in Section IV.

II. Method

An alternative method to determine the sea clutter on the receiving antenna of an HFSWR system is proposed. To apply the proposed method, the sea surface must be discretized into patches with dimensions in the order of a few wavelengths. The sea clutter will be determined from the sum of the complex value of the voltages induced by each individual patch. A scheme representing the arrangement of the patches and the trajectories of the incoming and outgoing signals is presented in Fig. 1.

In Fig. 1, three trajectories of the incoming and outgoing signals are shown by the way of an example. The incoming signal goes from the transmitting antenna (Tx) to the sea patch, while the outgoing signal goes from the patch to the receiving antenna (Rx). The trajectories shown in Fig. 1 correspond to the patches numbered 1, 8, and 12 and are associated to the

voltages U_1, U_8, and U_{12} induced on the receiving antenna. The sea clutter is obtained by summing the voltages U_i induced by all the patches on the receiving antenna.

The angles of the incoming and the outgoing trajectories are independently controlled. This allows the computation of the sea clutter for the monostatic and the bistatic case. For the monostatic case, both angles are made equal, while for the bistatic case, the angles are different.

The proposed method to determine the sea clutter will be applied to an HFSWR system aimed at maritime surveillance within the EEZ of France, which extends to distances of 370 km from the coasts. Therefore, a typical surveillance area of the radar has an area of 300 km $\times$ 1 km. As mentioned previously, the sea patches have extension of a few wavelengths (λ). If patches of 100 m $\times$ 100 m are used, which corresponds to an extension of $5\lambda \times 5\lambda$ at 15 MHz, the number of patches required to discretize the surveillance area would be 30 000. This large number of patches makes it necessarily an efficient method to calculate the voltage induced by each patch.

To obtain the voltage U_i induced by each patch, the Lorentz reciprocity theorem will be applied, as presented in the next section. By means of the Lorentz reciprocity theorem, the voltage U_i is computed from the electromagnetic fields observed in a surface surrounding the sea patch, known as Huygens surface [25]. These fields are of two types: diffracted fields, with the receiving antenna in reception mode, and incident fields, with the receiving antenna in emission mode. The diffracted fields are due to the diffraction phenomenon occurring on the surface of the sea patch, while the incident fields are independent of this phenomenon. In reality, the incident fields on a given patch also include fields diffracted by neighboring patches. However, for the characterization of a single patch, it can be assumed that the patches that surround it are completely flat and do not produce diffracted fields. This does not affect the precision of the method, since at the moment of considering all the sea patches together, the calculation of the incident field on each patch will be made by means of the parabolic equation [26], which takes into account the propagation effects and the fields diffracted by the neighboring patches. In this way, the authors will consider two different propagation effects: propagation attenuation in the paths between the emitting antenna and the patch, and between the patch and the receiving antenna, as well as the diffraction of each patch.

The system parameters that mainly affect the value of the fields on the Huygens surface are the following:

1) *Frequency of the wave*: It affects both diffracted and incident fields.
2) *Sea state*: specified, for example, in the Beaufort scale [27], it affects only the diffracted fields.
3) *Angle of the incoming trajectory*: It affects the diffracted fields.
4) *Angle of the outgoing trajectory*: It affects the incident fields.
5) *Distance between the patch and the antennas*: It affects both diffracted and incident fields.

The principle of the proposed method is the determination of the voltage U_i induced by any patch, from the characterization of one single patch, for different values of the previously listed system parameters.

The characterization of these parameters is done as indicated in the following.

1) To consider the distance and the profile of the sea surface between the patch and the antennas, the parabolic equation [26] is used. This equation considers the phenomena of propagation and diffraction of electromagnetic waves, thus allowing the calculation of the electric field in the center of each patch, for a given value of the input field at the terminals of the transmitting antenna. Then, the antennas are replaced by plane wave sources with electric field amplitude of 1 V/m. The fields on the Huygens surface originated by the plane waves are multiplied by the electric field in the center of each patch.
2) For a given frequency and sea state, several simulations are done for different values of the angles of the incoming and the outgoing trajectories. For each angle of the incoming trajectory, a set of diffracted fields is obtained on the Huygens surface. Then, this set of diffracted fields is combined with the incident fields calculated for each value of the angle of the outgoing trajectory. This combination of diffracted and incident fields is done according to the Lorentz reciprocity theorem, as explained in the following section.

To be able to compute the voltage induced by any patch, from the characterization of one single patch, many simulations are required, for different combinations of the system parameters. Since the induced voltage is computed from the fields on the Huygens surface by means of the Lorentz reciprocity theorem, the problem is reduced to get a way to predict the shape of the fields on the Huygens surface for different values of the system parameters. To do this, the field distribution on the Huygens surface is approximated by means of analytical expressions. Then, the variation of each coefficient of these analytical expressions must be found as a function of the system parameters. In this way, the voltages induced by all the sea patches can be obtained and added to give rise to the sea clutter.

This article presents the method to approximate the fields on the Huygens surface by means of analytical expressions and the way in which the fields reconstructed from these expressions allow to calculate, with an acceptable error, the value of the voltage induced on the receiving antenna, by means of the Lorentz reciprocity theorem. Additionally, it is shown that the antennas can be replaced by plane wave sources to simplify the analysis and that the Doppler spectrum can be obtained from the time evolution of the induced voltage.

Next, the Lorentz reciprocity theorem is described, as it is the basic element for the calculation of the voltage induced on the receiving antenna from the fields on the Huygens surface.

A. Lorentz Reciprocity Theorem

To determine the induced voltage at the port of the receiving antenna (U_a^{rec}) from the electromagnetic fields diffracted by the sea patch, the Lorentz reciprocity theorem is applied [24]. To do this, the structure presented in Fig. 2 is simulated in the electromagnetic simulation software Altair FEKO.

The transmitting and the receiving antennas are implemented as monopoles of length $\lambda/4$, where $\lambda = 20$ m is the wavelength at

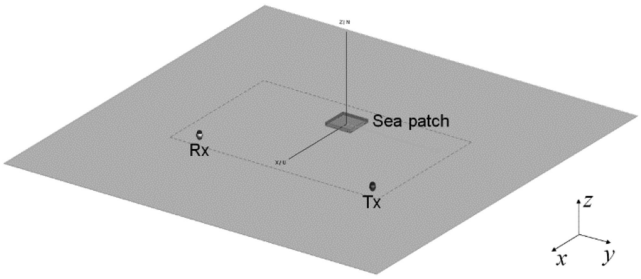

Fig. 2. Simulated structure including the transmitting antenna (Tx), the receiving antenna (Rx), and the sea patch.

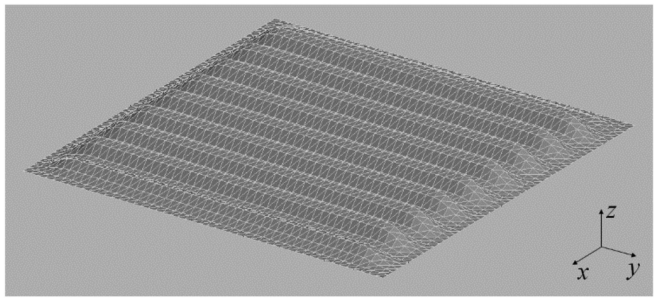

Fig. 3. Sea patch with smooth borders to get a value of zero height at the ends.

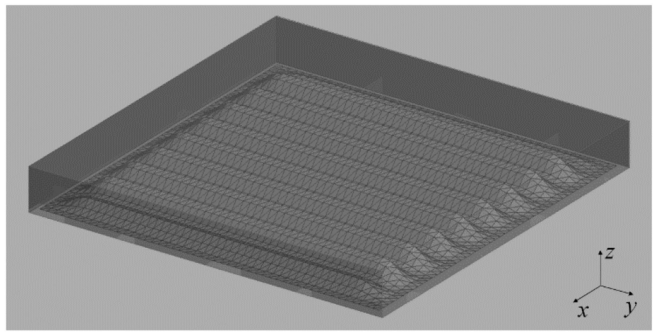

Fig. 4. Huygens surface surrounding the sea patch.

15 MHz. The sea patch is centered on the origin of the coordinate system. The distance between each antenna and the origin is 500 m. The transmitting antenna is located at an azimuth angle of ϕ_i, while the azimuth angle of the receiving antenna is $-\phi_i$. A perfect electric ground plane covers the entire region under the monopoles and the patch so that, in the simulation, the patch and its image are considered [27].

The patch extends along the *x*- and *y*-directions with the sea height in the *z*-direction. The dimensions of the patch in the *x*–*y* plane are 100 m × 100 m. For simulation efficiency, the media used for the patch is perfect electric conductor. The sea height, $h(x, y)$, is taken as that of a sinusoidal surface invariant in the *y* direction, with period $\lambda_v = \lambda/2$, given by

$$h\,(x, y) = A\ \sin\left(\frac{2\pi x}{\lambda_v}\right) + 3\frac{A}{2}. \tag{1}$$

The amplitude A of the sinusoidal surface in (1) is chosen to be 2.0125 m to represent the significant height of the sea state given by the scale 5 of Beaufort [27]. The constant level of $3A/2$ is added in (1) to make all height values positive. It is required to form the surface image at the other side of the ground plane.

To reduce the effects of the patch borders on the diffraction phenomenon, these have been smoothed by multiplying the sea height by the sine squared and cosine squared functions presented in (2) and (3). The multiplication is done on the 1-D sea profiles in the *x*- and *y*-directions.

In (2) and (3), r is the distance in *x*- or *y*-directions, l_{trans} is the distance used to do the transition at both ends of the patch, r_{ini} is the initial point of the patch, and r_{fin} is the final point of it. By multiplying the patch by the functions in (2) and (3), a zero height value is obtained at the ends of the patch, as shown in Fig. 3.

The sea patch is surrounded by a Huygens surface *S*, where the electromagnetic fields are stored. In this case, the Huygens surface is constituted by the five faces of a box that are not in contact with the ground plane, as shown in Fig. 4. The edges of this box are located at $\lambda/20 = 1$ m from the patch ends in the *x*–*y* plane, which makes the box to measure 102 m × 102 m in this plane. In the *z*-direction, the height of the box is 12 m. According to (1), the maximum patch height is 5.0313 m, then, the edge of the box in the *z*-direction is located at 6.9687 m from the maximum patch height. The electromagnetic fields are stored on the Huygens surface, in the nodes of the discretization grid given by the following spatial steps: $\Delta x = 0.9902$ m, $\Delta y = 0.9902$ m, and $\Delta z = 0.3$ m, which corresponds to 104 observation points in *x*, 104 in *y*, and 41 in *z*.

$$\sin^2(r) = \begin{cases} \sin^2\left(\frac{\pi}{2}\left(\frac{r-r_{\text{ini}}}{l_{\text{trans}}}\right)\right), & r_{\text{ini}} \le r \le r_{\text{ini}} + l_{\text{trans}} \\ 1, & r_{\text{ini}} + l_{\text{trans}} < r \le r_{\text{fin}} \end{cases} \tag{2}$$

$$\cos^2(r) = \begin{cases} 1, & r_{\text{ini}} \le r < r_{\text{fin}} - l_{\text{trans}} \\ \cos^2\left(\frac{\pi}{2}\left(\frac{r-(r_{\text{fin}}-l_{\text{trans}})}{l_{\text{trans}}}\right)\right), & r_{\text{fin}} - l_{\text{trans}} \le r \le r_{\text{fin}}. \end{cases} \tag{3}$$

The Lorentz reciprocity theorem is based on two states of the receiving antenna: the state of reception and the state of emission. In the state of reception, the transmitting antenna emits energy and the fields diffracted by the sea patch are stored in the surface *S*. In the state of emission, the sea patch is removed from the simulated geometry, the receiving antenna emits energy and the incident fields are stored in the surface *S*. The Lorentz reciprocity theorem is given by

$$U_a^{\text{rec}} = -\frac{Z_{\text{in}} Z_L}{U_a^{\text{emi}}\,(Z_{\text{in}} + Z_L)} \times \left(\sum_{\text{mesh}} \hat{n} \times \vec{H}_c^{\text{rec}} \cdot \vec{E}_c^{\text{emi}} \Delta s - \sum_{\text{mesh}} -\hat{n} \times \vec{E}_c^{\text{rec}} \cdot \vec{H}_c^{\text{emi}} \Delta s\right) \tag{4}$$

where

U_a^{rec} induced voltage at the receiving antenna in reception mode;

Z_{in} input impedance of the receiving antenna in emission mode;

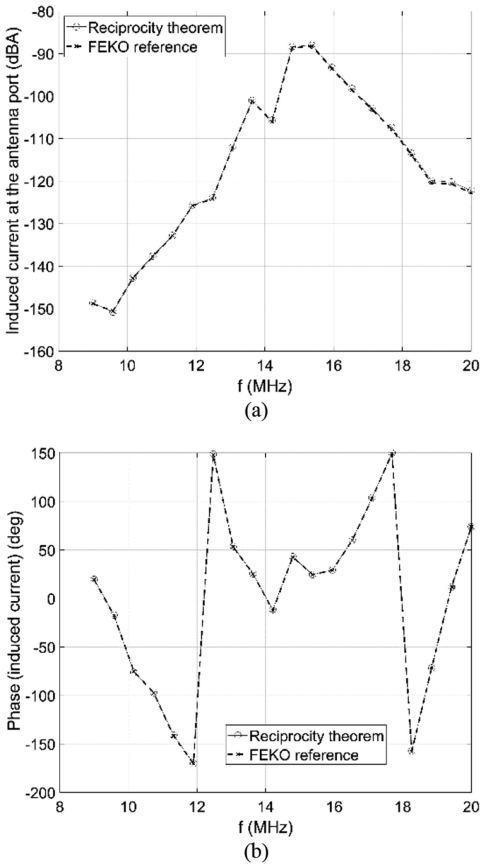

Fig. 5. Induced current at the receiving antenna for incidence angle $\phi_i = 30°$. (a) Magnitude. (b) Phase.

Z_L load impedance of the receiving antenna in reception mode;
U_a^{emi} excitation voltage of the receiving antenna in emission mode;
$\hat{n}$ inward unit normal vector;
$\vec{H}_c^{\mathrm{rec}}$ magnetic field on the Huygens surface in reception mode;
$\vec{E}_c^{\mathrm{emi}}$ electric field on the Huygens surface in emission mode;
Δs area of the discretization cell on the Huygens surface;
$\vec{E}_c^{\mathrm{rec}}$ electric field on the Huygens surface in reception mode;
$\vec{H}_c^{\mathrm{emi}}$: magnetic field on the Huygens surface in emission mode.

The induced voltage at the receiving antenna, U_a^{rec}, is computed by means of (4) and the induced current I_a^{rec} is obtained as U_a^{rec}/Z_L. To validate the results obtained from the Lorentz reciprocity theorem, these are compared with the induced current directly computed by FEKO. This comparison is presented in Fig. 5, where the induced current obtained from the Lorentz reciprocity theorem is compared with that computed by FEKO. The current in Fig. 5 corresponds to an angle of incidence $\phi_i = 30°$ and is computed for 20 linearly spaced frequencies between 9 and 20 MHz. The magnitude of the current in Fig. 5(a) is presented in dBA to better observe the agreement between the two results.

TABLE I
FIELD COMPONENTS THAT CONTRIBUTE TO THE CALCULATION OF THE INDUCED VOLTAGE

Face	Dominant field components	Secondary field components
yz_front	E_z, H_y	E_y, H_z
yz_back	E_z, H_y	E_y, H_z
xz_right	E_z, H_x	E_x, H_z
xz_left	E_z, H_x	E_x, H_z
xy_top	E_x, E_y, H_x, H_y	--

The current computed from the Lorentz reciprocity theorem is in good agreement with the reference value given by FEKO, in magnitude and phase, for all the frequencies presented in Fig. 5. The two curves overlap almost in all frequencies. In this way, the method to compute the induced current by means of the Lorentz reciprocity theorem has been validated and can be used to compute this current from the electromagnetic field distribution obtained in the Huygens surface.

B. Interpolation of Field Charts

To determine the sea clutter, we start from the voltage induced at the receiving antenna by one single patch. Then, the contributions of the other patches will be added. As stated in the previous section, the induced voltage is computed from the electromagnetic field distribution in the Huygens surface, or field charts, by means of the Lorentz reciprocity theorem. As explained in the previous section and illustrated in Fig. 4, the Huygens surface consists of five faces of a box surrounding the sea patch. According to (4), only the tangential components of the fields are used in each of these faces to compute the induced voltage. In Fig. 4, it is seen that these faces are aligned with the coordinate axes, then, we will name these surfaces as follows.

1) *yz_front*: Front face, in the *y*–*z* plane.
2) *yz_back*: Back face, in the *y*–*z* plane.
3) *xz_right*: Right side face, in the *x*–*z* plane.
4) *xz_left*: Left side face, in the *x*–*z* plane.
5) *xy_top*: Top face, in the *x*–*y* plane.

The transmitting antenna is a monopole λ/4 oriented in the *z*-direction, then, the radiated electric field is polarized in the *z*-direction, while the magnetic field is polarized in the *x*–*y* plane. This allows formulating the hypothesis that on each face of the Huygens surface, the dominant field components are those aligned with the fields radiated by the monopole and the other field components, that we call secondary field components, are not significant when calculating the voltage induced at the receiving antenna. The list of the field components that contribute to the calculation of the induced voltage by means of the Lorentz reciprocity theorem (4), classified in dominant and secondary field components, for each face of the Huygens surface is presented in Table I.

In the face *xy_top* even the field components E_x and E_y, which are not aligned with the E_z field radiated by the monopole, are significant. This is because the E_z component does not contribute to the induced voltage in this face, since this is not a tangential component.

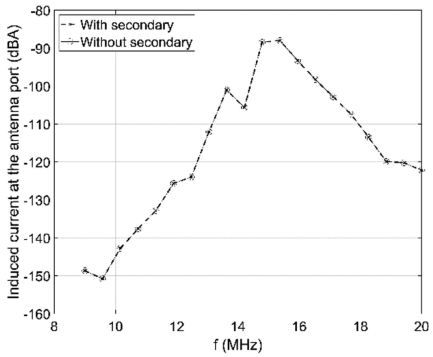

Fig. 6. Magnitude of the induced current with and without consideration of secondary components, for incidence angle $\phi_i = 30°$.

To validate the hypothesis about the insignificance of secondary components, the magnitude of the induced current at the receiving antenna was computed with and without consideration of these components. The results are plotted in Fig. 6.

In Fig. 6, it is seen that the two curves overlap. Then, the magnitude of the induced current is the same with and without consideration of secondary components. This confirms the hypothesis that secondary components can be neglected.

After neglecting the secondary components, and according to Table I, to compute the induced voltage only two field components are required in the four lateral faces: *yz_front, yz_back, xz_right,* and *xz_left*, while in the top face, four field components are required. These components are the ones that must be interpolated in each of the faces in order to calculate the induced voltage. The procedure of interpolation is described in the following for the four lateral faces and the top face.

1) Interpolation in the Four Lateral Faces: As stated previously, two field components must be interpolated in each lateral face (see Table I). This means that, four field charts must be interpolated in each face, since there is a real and an imaginary part for each field component.

The field charts of the lateral faces present sinusoidal variation in the longitudinal direction (*x*- or *y*-direction) and a monotonically decreasing variation in the vertical direction (*z*-direction). Thus, field variation can be independently interpolated in the longitudinal and vertical direction. Finally, these two independent interpolations are multiplied point by point to obtain the interpolation in the 2-D lateral face.

*a) Interpolation in the longitudinal direction (*x- *or* y-*direction):* The longitudinal field profile to be interpolated is taken at $z = 1$ m. This is because the sinusoidal variation is clearer near the ground plane ($z = 0$ m). The sinusoidal variation is approximated by the function $p_l(\xi)$ in (5), where ξ represents the variable *x* or *y*, depending on whether the face is in the *x*–*z* or *y*–*z* plane, respectively.

$$p_l(\xi) = a_1 \ \sin(k_1\xi + \phi_1) + a_2 \ \sin(k_2\xi + \phi_2). \quad (5)$$

There are six coefficients to be determined in (5) in order to fit the field profile: a_1, k_1, ϕ_1, a_2, k_2, and ϕ_2. These coefficients are initially determined by means of a Fourier transform of the field profile. The highest two peaks of the Fourier transform are taken to extract from them the value of the six coefficients. Then, an optimization process is run on these coefficients to better fit the field profile. In this case, the best fitting of the field profile was achieved by optimizing the value of the following two coefficients.

1) Phase of the first sine function: ϕ_1.
2) Phase of the second sine function: ϕ_2.

*b) Interpolation in the vertical direction (*z*-direction):* The field profile to be interpolated is taken at the value of the longitudinal variable (*x* or *y*), where the longitudinal field profile is maximum. The decreasing variation is approximated by the second-degree polynomial, $p_v(z)$, as

$$p_v(z) = c_2 z^2 + c_1 z + c_0. \quad (6)$$

The three coefficients c_0, c_1, and c_2 in (6) are determined by means of the polynomial fitting function "polyfit" of the software MATLAB.

c) Interpolation in the lateral face: The interpolation in the lateral face, $p_{\text{lat}}(\xi, z)$, is done by multiplying point by point the interpolation in the longitudinal direction by the interpolation in the vertical direction, as stated in the following equation:

$$p_{\text{lat}}(\xi, z) = p_l(\xi)\, p_v(z). \quad (7)$$

An example of interpolation in a lateral face is presented in the following. The example is done for the real part of the H_y component, in the *yz_front* face, at a frequency of 15.37 MHz and an angle of incidence $\phi_i = 30°$.

The interpolation in the longitudinal and the vertical direction are presented in Fig. 7(a) and (b), respectively.

In Fig. 7(a), the interpolation in the longitudinal direction presents a good agreement with the original profile in terms of period and phase. The discrepancies in amplitude are tolerable since they do not significantly affect the value of the voltage induced on the receiving antenna. In Fig. 7(b), it is observed that a second-degree polynomial adequately predicts the variation of the field in the vertical direction. To fit exactly the field profile, a higher degree polynomial could be used, however, for the simplicity of the interpolation model, a second-degree polynomial is more convenient.

After obtaining the interpolation functions for the longitudinal and the vertical profile, the interpolation of the complete field chart is determined by multiplying point by point the longitudinal and vertical interpolations, as stated in (7). The so obtained interpolated field chart is compared with the original one in Fig. 8.

As can be seen in Fig. 8, the interpolated chart does not exactly reproduce the original chart. The form of interpolation used, by multiplying two perpendicular profiles, does not allow reproducing some variations of the chart, such as the local maximum observed in the upper left of Fig. 8(a).

However, the overall variation of the field is reproduced adequately. When calculating the induced voltage in the receiving antenna by means of the Lorentz reciprocity theorem, a reproduction of the original chart as that observed in Fig. 8 does not produce significant error in the value of the voltage.

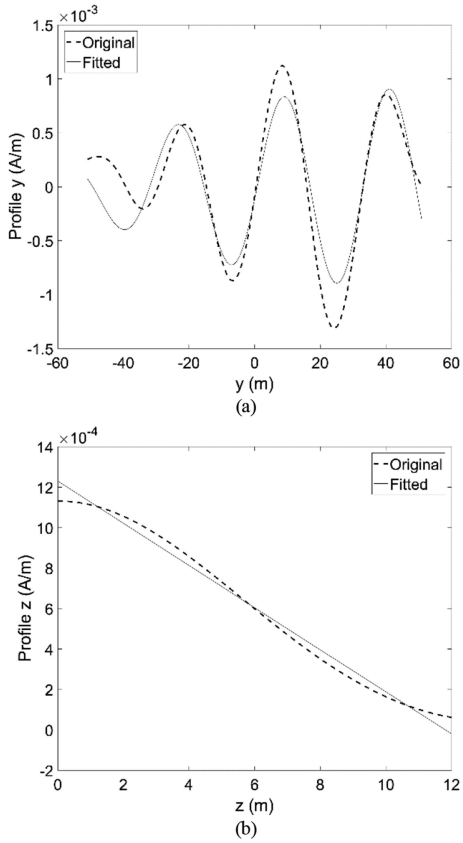

Fig. 7. Interpolation of the Real(H_y) field component in the lateral face *yz_front* at $f = 15.37$ MHz and $\phi_i = 30°$. (a) Longitudinal direction. (b) Vertical direction.

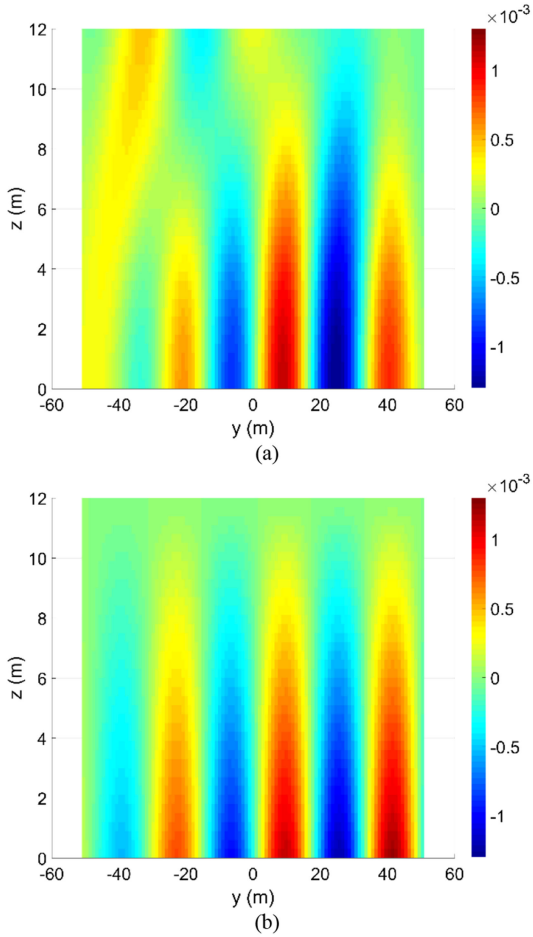

Fig. 8. Field charts of the Real(H_y) component in the lateral face *yz_front* at f = 15.37 MHz and $\phi_i = 30°$. (a) Original chart. (b) Interpolated chart.

2) Interpolation in the top face: According to Table I, four field components (E_x, E_y, H_x, and H_y) must be interpolated in the top face, which corresponds to the interpolation of eight field charts, two for each field component, representing the real and imaginary parts.

Unlike the lateral faces, the field charts of the top face do not present independent variation in two perpendicular directions. For this reason, the interpolation must be done as a function of the two directions of variation of the face, "*x*" and "*y.*"

The field variation in the charts is approximated by the function $p_{\text{top}}(x, y)$ as follows:

$$p_{\text{top}}(x,y) = a_1 \sin\left[k_1\left(\cos\theta_1 x + \sin\theta_1 y\right) + \phi_1\right] + a_2 \sin\left[k_2\left(\cos\theta_2 x + \sin\theta_2 y\right) + \phi_2\right]. \quad (8)$$

There are eight coefficients to be determined in (8) to fit the field chart: a_1, k_1, θ_1, ϕ_1, a_2, k_2, θ_2, and ϕ_2. To determine the value of six of these eight coefficients ($a_1, k_1, \theta_1, a_2, k_2$, and θ_2) the 2-D Fourier transform of the field chart is computed. The value of these six coefficients is extracted from the two highest peaks of the Fourier transform. The remaining two coefficients (ϕ_1, ϕ_2) are determined by means of an optimization process aimed at improving the fitting of the field chart.

An example of interpolation in the top face is presented in the following. The example is done for the real part of the H_y component at a frequency of 14.21 MHz and an angle of incidence $\phi_i = 30°$. The interpolated field chart obtained after the optimization process of the fitting function in (8) is compared to the original chart in Fig. 9.

The interpolated chart in Fig. 9(b) presents the same field variation of the original chart in Fig. 9(a), except for the attenuation function observed in the incidence direction of the wave and in the direction perpendicular to this incidence. The form of the interpolation function in (8) does not consider these attenuations. The incorporation of the attenuations to the interpolation model increases the degree of complexity of it. This is not convenient when considering that the objective is to predict the variation of the interpolation coefficients in terms of different system parameters. For this reason, it was decided to work with the interpolation function in (8).

III. Results

The objective is to demonstrate the feasibility of using analytical expressions to approximate the field charts on each of the faces of the Huygens surface and to calculate the voltage induced on the receiving antenna from the reconstructed charts, by means of the Lorentz reciprocity theorem.

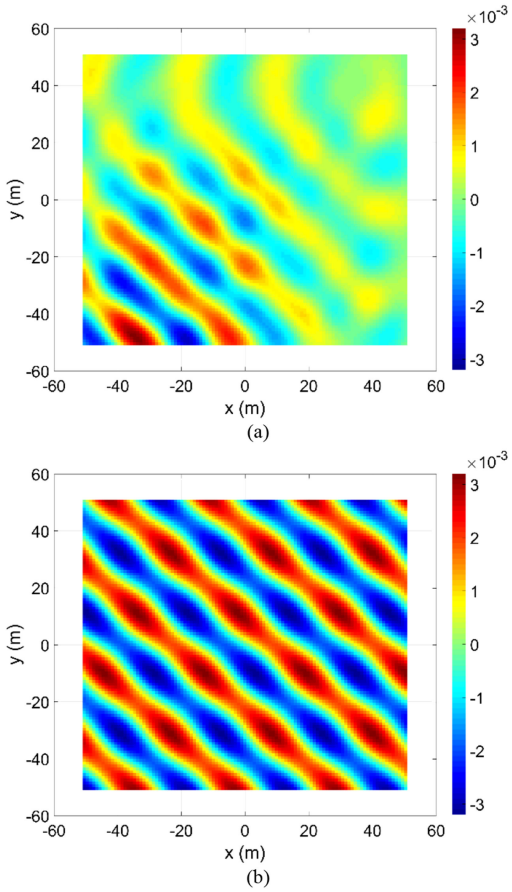

Fig. 9. Field charts of the Real(H_y) component in the top face *xy_top* at f = 14.21 MHz and $\phi_i = 30°$. (a) Original chart. (b) Interpolated chart.

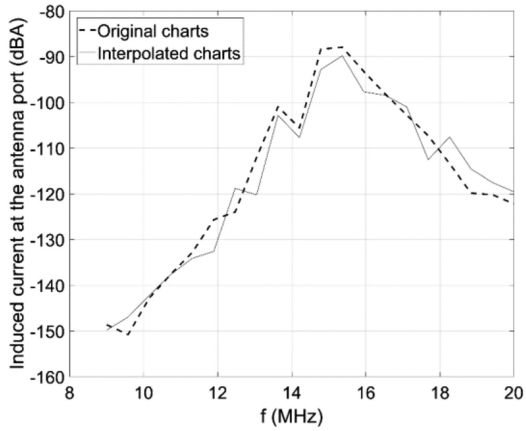

Fig. 10. Magnitude of the induced current computed from the original and the interpolated charts, for incidence angle $\phi_i = 30°$.

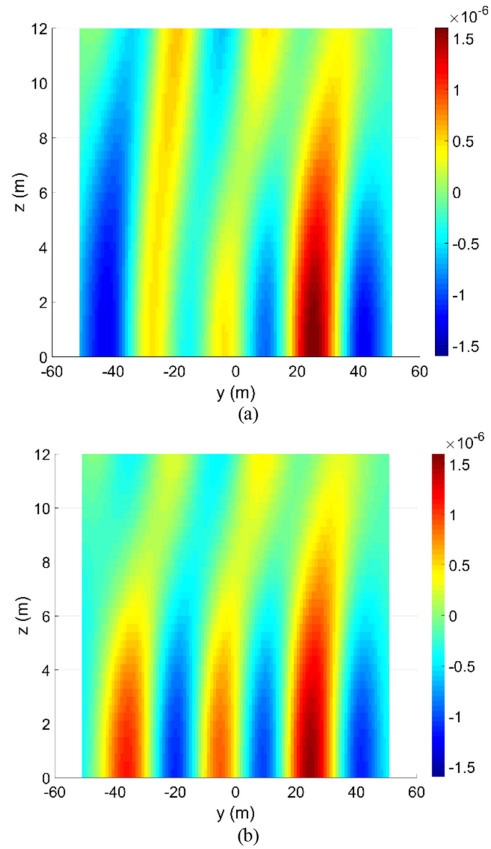

Fig. 11. Field charts of the Real(H_y) component in the front face *yz_front* at f = 14.50 MHz and $\phi_i = 45°$. (a) Antenna excitation. (b) Plane wave excitation.

With this objective in mind, the field charts for the four lateral faces and the top face were interpolated as described in the previous section, for 20 frequencies equally spaced between 9 and 20 MHz. Subsequently, the interpolated charts were used to calculate the voltage induced on the receiving antenna by means of the Lorentz reciprocity theorem (4). The physical parameters of the simulated geometry are the same of that presented in Section II.

The magnitude of the induced current at the antenna port computed from the interpolated charts is compared with that computed from the original charts in Fig. 10.

The induced current calculated from the interpolated charts fits properly that calculated from the original charts. The differences between the two curves are due to the approximation error made when reconstructing the charts from the analytical expressions. However, this error is tolerable if it is considered that for the final computation of the sea clutter, the sum of the currents induced by all the sea patches is required. The number of sea patches for a surveillance area of 300 km × 1 km is in the order of 30 000. Therefore, the errors made in the calculation of the current induced by a patch are compensated by doing the summation on such a large number of patches.

To simplify the calculation of the fields that take part in the Lorentz reciprocity theorem (4), it is convenient to replace the transmitting and receiving monopole antennas by plane wave sources. Considering that the field radiated by a monopole in the far field region can be approximated by a plane wave, the resulting field charts on the faces of the Huygens surface should not change much if the excitation is done with monopole antennas or plane waves. To verify this assumption, in Figs. 11 and 12, the field charts produced by these two excitations are compared, for the components Real(H_y) and Real(E_z), respectively. These charts correspond to the front face *yz_front*, at the frequency of 14.50 MHz, for an angle of incidence $\phi_i = 45°$.

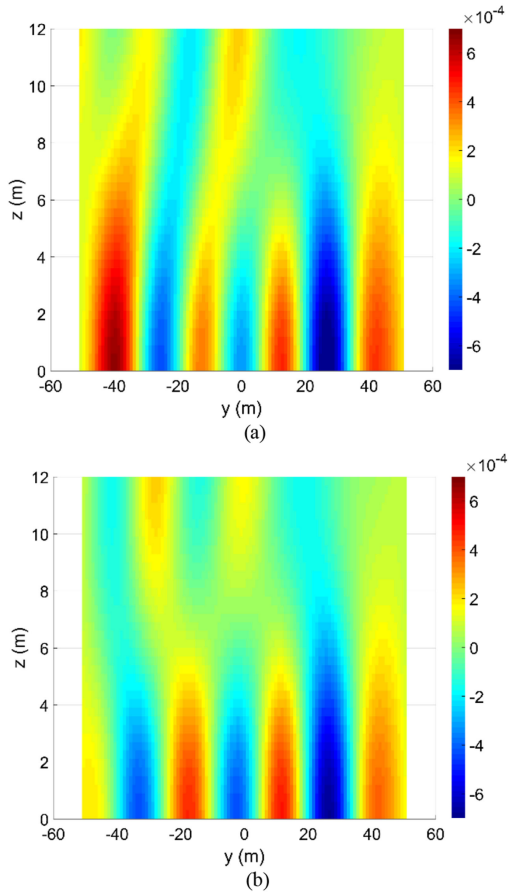

Fig. 12. Field charts of the Real(E_z) component in the front face *yz_front* at f = 14.50 MHz and $\phi_i = 45°$. (a) Antenna excitation. (b) Plane wave excitation.

Although the field charts compared in Figs. 11 and 12 are not exact, they do present a high similarity, especially in the region of positive y, which corresponds to the region on which the transmitted wave strikes the Huygens surface (see Fig. 2). In the region of negative y, the dominant fields are no longer those due to the transmitted wave, but those diffracted by the sea patch.

Despite the differences in the field charts, to verify if the antennas can be replaced by plane wave sources, we proceed to calculate the induced current, by means of the Lorentz reciprocity theorem. This is done from the field charts in the five faces of the Huygens surface, for the cases of excitation with antenna and plane wave, for 20 frequencies between 9 and 20 MHz. The results are presented in Fig. 13.

In Fig. 13, it is confirmed that for purposes of induced current calculation, the excitation by antenna is practically equivalent to the excitation by plane wave. Significant differences are observed only at two frequencies, 15.6 and 17.8 MHz. However, these differences fall within the range of tolerable error that is compensated when summing the voltages induced by all sea patches.

Finally, to validate the proposed method of sea clutter computation, the Doppler spectrum is calculated for a sea surface in motion. The sea surface height follows a Jonswap spectrum [28] with wind direction $\theta_0 = 10°$ and Beaufort scale 4 with

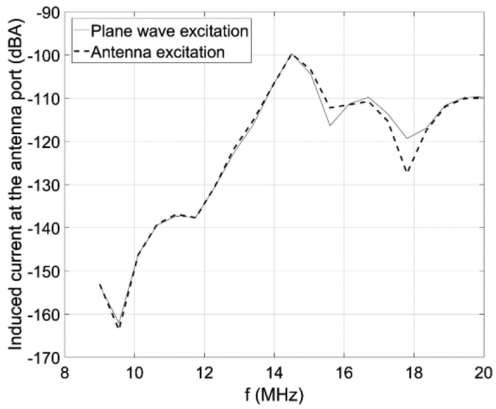

Fig. 13. Magnitude of the induced current computed with plane wave and antenna excitation, for incidence angle $\phi_i = 45°$.

wind friction velocity $u_f = 19\,\mathrm{cm/s}$. The Doppler spectrum is calculated as the Fourier transform of the voltage at the receiving antenna, and in turn, this voltage is calculated by means of the Lorentz reciprocity theorem, as presented previously. The calculation is made for the monostatic case at a frequency $f_r = 15\,\mathrm{MHz}$. The analyzed sea surface is a 256 m × 256 m patch.

The size of the surface was chosen by considering that it must be large enough to be statistically representative of the sea state. This means that two different realizations of the sea surface must be similar from a statistical point of view [27]. Intuitively a surface with size of some wavelengths is needed. This size corresponds to a region of strong correlation. To ensure the statistical representativeness of the sea surface, an analysis of two characteristic statistical properties of a rough surface is done in [27]. These properties are the correlation length (L_c) and the mean square height (h_{rms}). In [27], L_c is calculated for a sea surface with JONSWAP spectrum, with Beaufort 4 sea state and wind friction velocity $u_f = 19\,\mathrm{cm/s}$ at 15 MHz, and the convergence of h_{rms} is evaluated as a function of the surface size. After this analysis, it is found that the minimum dimensions of the sea surface, to be statistically representative, are 180 m × 180 m. The size of the surface to be simulated was chosen in 256 m × 256 m in order to facilitate the calculation of the fast Fourier transform (FFT), having a number of points that are power of 2. The FFT is necessary at the time of calculating the rough surface from its JONSWAP spectrum.

The temporal evolution of the sea surface is observed in time steps $dt = 0.25\,\mathrm{s}$, during a total time of 75 s, which implies the simulation of 300 sea surfaces to obtain the voltage induced on the antenna in each time step. The waves of the sea surface propagate toward the antenna. The obtained Doppler spectrum is presented in Fig. 14.

As shown in Fig. 14, the Bragg ray appears at $f_B = +0.39\,\mathrm{Hz}$, as expected for a surface propagating toward the antenna at a frequency $f_r = 15\,\mathrm{MHz}$, considering (9), presented in [27].

$$f_B \approx 0.1\sqrt{f_r\,[\mathrm{MHz}]}. \tag{9}$$

In [27] a Doppler spectrum is computed for a sea surface with the same characteristics of that simulated in Fig. 14, except for

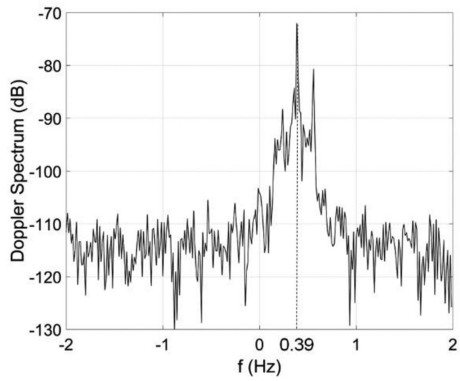

Fig. 14. Doppler spectrum for a Jonswap sea surface ($\theta_0 = 10°$, $u_f = 19\,\mathrm{cm/s}$) of 256 m × 256 m in the monostatic case, $f_r = 15\,\mathrm{MHz}$, $\mathrm{d}t = 0.25\,\mathrm{s}$, observation time 75 s, propagation toward the antenna.

the dimensions, which are not 256 m × 256 m but 180 m × 180 m. In spite of this difference, the spectrum of Fig. 14 is very similar to that of [27], especially in the position of the Bragg ray at 0.39 Hz. However, in the spectrum of [27], there are strong components at 0 Hz, which are not observed in Fig. 14. These fictitious components are attributed in [27] to the smoothing of the borders of the simulated sea surface. Therefore, these components are numerical artifacts and they are nonphysical. It is the consequence of the surface truncation. Since the truncated region does not move, a Doppler is numerically observed at 0 Hz. The smoothing of the borders is also done on the sea surface simulated in Fig. 14, as given by the sine-squared and cosine-squared functions of (2) and (3). In spite of such smoothing, the spectrum of Fig. 14 does not have the components at 0 Hz reported in [27]. It indicates that the proposed method for the computation of the induced voltage does not generate fictitious 0-Hz components, in opposition to the method used in [27], which is the method of integral equations solved by the method of moments.

In this way, the computation method of the voltage induced on the receiving antenna is validated. This method is what allows to characterize the sea clutter, by adding the voltages induced by all the patches.

IV. Conclusion

This article shows the validation of the procedure for calculating the induced current on the receiving antenna of an HFSWR from the fields diffracted by each sea patch. Additionally, the diffracted field charts on the Huygens surface have been modeled by simple analytical expressions. It has also been shown that the fields reconstructed through these expressions allow calculating the induced current with an acceptable error and that the transmitting and receiving antennas can be replaced by plane wave sources, to simplify the calculation of the radiated fields. The computation procedure of the induced voltage has been satisfactorily applied for the calculation of the Doppler spectrum of a Jonswap sea surface in motion. To do this, the induced voltage has been computed in 300 simulations representing the state of the sea surface at each observed time step.

As future work, multiple simulations are planned for different values of the following system parameters: frequency, magnitude of the wind vector, wind direction, and azimuthal angle of the incident wave. The magnitude of the wind vector establishes the amplitude of the sea waves and the wind direction translates into a direction of sea wave propagation. After performing these simulations, the diffracted field charts can be modeled through the expressions presented in this article. The variation of the coefficients of these expressions will be analyzed as a function of each system parameter, in order to fit a metamodel to that variation. Once this metamodel is adjusted, the field charts can be calculated for any value of the system parameters. In this way, it will be possible to calculate the total induced current on the receiving antenna, obtained from the sum of all the currents induced by each sea patch.

References

[1] L. Sevgi, A. Ponsford, and H. C. Chan, "An integrated maritime surveillance system based on high-frequency surface-wave radars. 1. Theoretical background and numerical simulations," *IEEE Antennas Propag. Mag.*, vol. 43, no. 4, pp. 28–43, Aug. 2001.

[2] D. E. Barrick, "Grazing behaviour of scatter and propagation above any rough surface," *IEEE Trans. Antennas Propag.*, vol. 46, no. 1, pp. 73–83, Jan. 1998.

[3] D. Barrick, "Theory of HF and VHF propagation across the rough sea, 1, The effective surface impedance for a slightly rough highly conducting medium at grazing incidence," *Radio Sci.*, vol. 6, no. 5, pp. 517–526, 1971.

[4] D. Barrick, "Theory of HF and VHF propagation across the rough sea, 2, application to HF and VHF propagation above the sea," *Radio Sci.*, vol. 6, no. 5, pp. 527–533, 1971.

[5] E. W. Gill and J. Walsh, "A perspective on two decades of fundamental and applied research in electromagnetic scattering and high frequency ground wave radar on the Canadian east coast," in *Proc. IEEE Int. Geosci. Remote Sens. Symp.*, Toronto, ON, Canada, 2002, pp. 521–523.

[6] E. Gill and J. Walsh, "High-frequency bistatic cross section of the ocean surface," *Radio Sci.*, vol. 36, no. 6, pp. 1459–1475, 2001.

[7] E. Gill, W. Huang, and J. Walsh, "On the development of a second-order bistatic radar cross section of the ocean surface: A high-frequency result for a finite scattering patch," *IEEE J. Ocean. Eng.*, vol. 31, no. 4, pp. 740–750, Oct. 2006.

[8] D. Barrick, "First-order theory and analysis of MF/HF/VHF scatter from the sea," *IEEE Trans. Antennas Propag.*, vol. 20, no. 1, pp. 2–10, Jan. 1972.

[9] J. Walsh, W. Huang, and E. Gill, "The first-order high frequency radar ocean surface cross section for an antenna on a floating platform," *IEEE Trans. Antennas Propag.*, vol. 58, no. 9, pp. 2994–3003, Sep. 2010.

[10] E. Gill, "The scattering of high frequency electromagnetic radiation from the ocean surface: An analysis based on a bistatic ground wave radar configuration," Ph.D. thesis, Fac. Eng. Appl. Sci., Memorial Univ. Newfoundland, St. John's, NL, USA, 1999.

[11] L. Vaitilingom and A. Khenchaf, "Radar cross sections of sea and ground clutter estimated by two scale model and small slope approximation in HF-VHF bands," *Prog. Electromagn. Res., B*, vol. 29, pp. 311–338, 2011.

[12] P. Hermansson, G. Forssell, and J. Fagerström, "A review of models for scattering from rough surfaces," Swedish Defence Research Agency, Sensor Technology, Linköping, Sweden, Tech. Rep., 2003.

[13] J. Jackson, *Classical Electrodynamics*. New York, NY, USA: Wiley, 1975.

[14] M. Nieto-Vesperinas, in *Scattering and Diffraction in Physical Optics*. New York, NY, USA: Wiley, 1991.

[15] L. Tsang, J. A. Kong, and K.-H. Ding, in *Scattering of Electromagnetic Waves, Theories and Applications*. New York, NY, USA: Wiley, 2000.

[16] L. Tsang and J. Kong, *Scattering of Electromagnetic Waves, Advanced Topics*. New York, NY, USA: Wiley, 2001.

[17] E. Thorsos and D. Jackson, "The validity of the perturbation approximation for rough surface scattering using a Gaussian roughness spectrum," *J. Acoust. Soc. Amer.*, vol. 86, no. 1, pp. 261–277, 1989.

[18] A. Khenchaf, "Bistatic scattering and depolarization by randomly rough surfaces: Application to the natural rough surfaces in X-band," *Waves Random Complex Media*, vol. 11, no. 2, pp. 61–89, 2000.

[19] A. Khenchaf, "Sea surface scattering for near-grazing incidence," in *Proc. Conf. MTS/IEEE Oceans*, Seattle, WA, USA, 1999, pp. 1452–1456.

[20] N. Sajjad, A. Khenchaf, and S. Mushtaq, "Grazing angle scattering of electromagnetic waves based on an improved two-scale model," *J. Appl. Remote Sens.*, vol. 7, no. 1, 2013.
[21] A. Voronovich, "Small-slope approximation in wave scattering by rough surfaces," *J. Exp. Theor. Phys.*, vol. 89, pp. 116–125, 1985.
[22] A. Voronovich, "Small-slope approximation for electromagnetic wave scattering at a rough interface of two dielectric half-spaces," *Waves Random Media*, vol. 4, no. 3, pp. 337–367, 1994.
[23] A. Voronovich, *Wave Scattering From Rough Surfaces*. Berlin, Germany: Springer-Verlag, 1994.
[24] H. Lorentz, "The theorem of Poynting concerning the energy in the electromagnetic field and two general propositions concerning the propagation of light," *Collected Papers*, vol. 3, pp. 1–15, 1936.
[25] A. Osipov and S. Tretyakov, *Modern Electromagnetic Scattering Theory With Applications*. Chichester, U.K.: Wiley, 2017.
[26] M. Levy, *Parabolic Equation Methods For Electromagnetic Wave Propagation*. London, U.K.: The Institution of Electrical Engineers, 2000.
[27] Y. Demarty, "Consistent modeling of electromagnetic scattering by of three-dimensional sea surfaces in grazing incidence. Application to HF surface wave radars," (in French), Ph.D. dissertation, Université Pierre et Marie Curie, Paris, France, 2008.
[28] K. Hasselmann, "Measurements of wind-wave growth and swell decay during the joint north sea wave project (JONSWAP)," (in German) *Deutsche Hydrographische Zeitschrift*, vol. A, no. 12, 1973.

Omar Nova was born on January 4, 1985, in Duitama, Colombia. He received the B.Sc. degree from the National University of Colombia, Bogotá, Colombia, in 2007, the M.Sc. degree from the University of Los Andes, Bogotá, in 2012, both in electronics engineering, and the Ph.D. degree in the framework of a double degree between the University of Los Andes, Bogotá, Colombia and Télécom Bretagne, Brest, France, in 2015.

Between September 2018 and August 2019, he had a Postdoctoral position with XLIM Institute, University of Limoges, Limoges, France. His research interests include electromagnetic compatibility, computational electromagnetics, and radio frequency and microwave engineering.

Christophe Guiffaut (Member, IEEE) received the master's and Ph.D. degrees in electronics and telecommunications from the University of Rennes, Rennes, France, in 1997 and 2000, respectively.

He joined the Centre National de la Recherche Scientifique Research Center in 2002 and integrated XLIM Laboratory, University of Limoges, Limoges, France, in 2002. His research interests include the numerical methods domain for application areas in electromagnetic compatibility, antennas, and ground penetrating radar.

Alain Reineix (Member, IEEE) received the master's degree in electronics and telecommunications and the Ph.D. degree in electronics from the University of Limoges, Limoges, France, in 1984 and 1986, respectively.

In 1986, he joined the Centre National de la Recherche Scientifique (CNRS) as a Researcher with the IRCOM Laboratory, University of Limoges. Since 1991, he has been a Research Director with the CNRS and also the Head of a Research Group on EMC, XLIM Institute Laboratory, France University of Limoges and has been with XLIM Institute, University of Limoges, since 2006. His current research interests include improvements on numerical modeling particularly in finite-difference time domain for electromagnetic compatibility applications and ground penetration studies in the radar domain.